ACS APPLIED POLYMER MATERIALS

pubs.acs.org/acsapm
Article

Architecturally Engineered Polyelectrolyte Binders: Property-Matching for Solid-State Battery Composite Cathodes

Zoé Lacour, Kanyapat Yiamsawat, and Georgina L. Gregory*

Cite This: ACS Appl. Polym. Mater. 2026, 8, 5459−5470
Read Online

ACCESS | Metrics & More | Article Recommendations | Supporting Information

ABSTRACT: Polymer binders in solid-state composite cathodes must provide ionic conductivity while maintaining mechanical integrity and interfacial contact, but the relative importance of these properties to battery performance is poorly understood. Here, we show that initial capacity for $LiNi_{0.8}Mn_{0.1}Co_{0.1}O_2/Li_6PS_5Cl/Li_4Ti_5O_{12}$ batteries correlates with polyelectrolyte binder ionic conductivity and interfacial resistance, while retention depends on plateau modulus (G_p') and damping factor (tanδ). Varying lithium borate polycarbonate with 10 wt % poly(ethylene oxide) (PEO) from linear to star and graft architectures generates conductivity-matched binder sets with distinct mechanical and interfacial properties. Linear binders combining high ionic conductivity (10^{-4} S cm^{-1}) and low interfacial resistance achieve the highest capacity (210 mAh g^{-1}), while graft architectures with long PEO side-chains deliver superior capacity retention (98% vs 92% for linear) through low G_p' (∼146 kPa) and high tanδ (∼0.8). Property-matching in one-dimension while using architecture to predictably vary others provides a generalizable design approach for multifunctional polymers in energy storage, extendable to solid polymer electrolytes and other systems requiring simultaneous optimization of transport and mechanical properties.

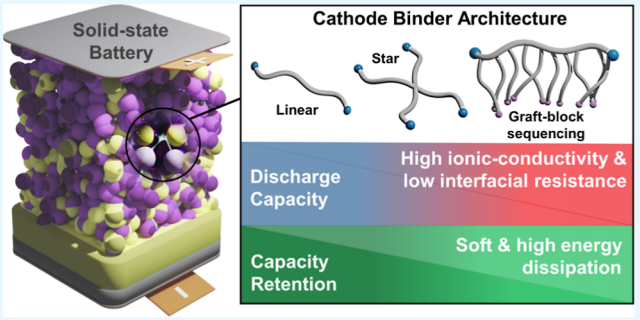

KEYWORDS: *polymer architecture, polyelectrolytes, single-ion conducting polymers, polycarbonate, ring-opening polymerization, block copolymers, star copolymers, graft polymers*

1. INTRODUCTION

Copolymer architectures such as linear, star, graft, and network structures provide a powerful tool to modulate polymer properties,[1−3] including ionic conductivity,[4,5] adhesiveness[6] and mechanical response.[7−9] These same properties are critical in determining the effectiveness of polymer binders for solid-state battery (SSB) composite cathodes,[10−14] the optimization of which is a current bottleneck in SSB performance.[15−17] While polymer-based solid electrolytes offer advantages in flexibility and interfacial compatibility,[18] sulfide-based solid electrolytes such as Li_6PS_5Cl provide ionic conductivities approaching liquid electrolytes (∼10^{-3} S cm^{-1} at 30 °C) and have driven the development of dry-processed composite cathodes, as sulfide electrolytes are sensitive to polar solvents. Dry processing requires polymeric binders that can form effective interparticle contact through mechanical mixing alone, placing demands on polymer deformability, adhesion and ionic conductivity.[19,20] Despite the alignment between architectural control of polymer properties and binder requirements, SSB binder design remains largely empirical, with most studies defaulting to linear architectures.[21] While ionically conductive polymers generally correlate with higher capacities,[22−24] and softer, more elastic and adhesive structures with better capacity retention,[25−29] these relationships prove more complex and difficult to predict in practice.[11] Ionic conductivity and mechanical properties typically covary, obscuring their relative importance to electrochemical performance.[29−31] Solid-state systems must maintain solid−solid interfaces during cycling at commercially viable stack pressures (<2 MPa),[32−34] accommodate volume changes without contact loss,[35] and enable efficient ion transport through thick electrodes.[16,36,37] Polymer architecture offers a parameter space for decoupling these competing demands, enabling systematic investigation of property-performance relationships.

While many studies on polymer electrolyte conductivities and mechanical profiles demonstrate the impact of architecture on the properties relevant for binder performance,[38−42] the challenge is to translate these bulk structure-property relationships to composite electrodes where the polymer comprises just 1−5 wt %. For ionic conductivity, poly(ethylene oxide)

Received: November 28, 2025
Revised: April 7, 2026
Accepted: April 7, 2026
Published: April 11, 2026

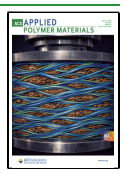

(PEO)-graft copolymers,[43−47] particularly with conductive polycarbonate backbones,[48] have achieved up to 3-fold higher conductivities than linear analogues, attributed to the less restricted mobility of PEO side-chains. Star architectures have similarly shown 1.5−2 times enhancement over linear polymers through increased free volume and reduced chain entanglement.[49] For mechanical response, highly grafted bottlebrush structures are associated with ultrasoft superelastic polymers,[7,50,51] with benefits to surface wettability and interfacial contact also reported,[6] while star architectures offer dimensional stability through covalent core junctions.[8,52] Importantly binders need to combine all these favorable properties, and various network architectures are promising such as cationic semi-interpenetrating networks that can also electrostatically aid dispersion of electrode components.[53]

Previous studies corroborating these architectural benefits in battery systems (e.g., star solid polymer electrolytes for low temperature cycling,[41,54] and graft polymers as superior solid electrolyte interphases at lithium anodes)[55] compare single architectures to linear controls. For binders, poly(vinylidene fluoride) (PVDF) grafted with poly(acrylic acid) (PAA) at optimized grafting ratio and side-chain interval was able to enhance capacity retention 30% compared to linear PVDF in high capacity Ni-rich cathodes.[6] Similarly, PAA-grafted carboxymethyl cellulose enabled 70% less fluorinated binder to be used while maintaining high cathode loadings (90 mg cm^{-2}).[56] Also, hyperbranched ionic conducting polymer binders accelerated polysulfide conversion in lithium−sulfur cells[57] and several examples of binders with network architectures have demonstrated better cycling stability: mechanically interlocked supramolecular structures achieved 1000 cycles in $LiFePO_4$ cathodes,[58] while interweaved networks stabilized $LiNi_{0.8}Mn_{0.1}Co_{0.1}O_2$ (NMC811) cathodes with 0.02% capacity fade per cycle.[59] While these studies demonstrate promising architectural benefits, they compare different chemistries and conditions, making it difficult to determine which property factors drive performance improvements. By generating conductivity-matched pairs with systematically varied architectures, we can isolate the contributions of mechanical and interfacial properties independent of ion transport.

Here, we synthesize PEO-polycarbonate block and gradient copolymers (90 wt % polycarbonate) with linear, star, and graft architectures via 2-allyloxymethyl-2-ethyltrimethylene carbonate (AEC)-cyclic carbonate ring-opening polymerization (ROP), converting them to lithium-ion conducting polyelectrolyte binders through lithium borate functionalization using thiol−ene chemistry and boron coordination. In general, thiol−ene chemistry has emerged as a versatile tool for functionalizing polymer battery components,[60] with demonstrated benefits particularly for adhesion in battery binder applications.[27,29] AEC monomer is advantageous for its one-step scalable synthesis (>100 g reported)[61] and the thiol−ene reactivity of the allyl group in the resulting polycarbonates is well established,[61−63] including UV-cross-linking to form polymer electrolyte films.[64] Our previous work exploited this chemistry on closely related 5-methyl-5-allyloxycarbonyl-1,3-dioxan-2-one (MAC)-based systems to prepare linear lithium borate polyelectrolyte binders with single-ion conductivity.[26] These single-ion conducting materials served as single-component binders, offering enhanced stability through anion immobilization, built-in adhesion via ionomer interactions, and mechanical networks through ionic cross-links. We now extend this approach to AEC-based linear (L), star (S), graft block (GB), and reverse-sequence graft gradient (GG) architectures across varying molar masses. Thermal, ionic conductivity (electrochemical impedance and dielectric relaxation spectroscopy), mechanical (rheology and compressive stress−strain), and adhesion (tack probe) characterization identify architectural pairs with matched ionic conductivities but differing mechanical properties, as well as pairs with similar mechanical properties but different ion transport characteristics. These binders are tested in dry-processed composite cathodes comprising single-crystal NMC811 (a high-capacity cathode material) and Li_6PS_5Cl (LPSCl, a high ionically conductive solid ceramic electrolyte). Cycling studies at 60 °C under 1 MPa over 100 cycles reveal capacity and capacity retention trends and architectural differences.

2. EXPERIMENTAL SECTION

2.1. General Procedure for Polyelectrolyte Synthesis

2.1.1. Block Copolymer Synthesis. The macroinitiator, e.g., α,ω-dihydroxy linear PEO (M_n = 10 kg mol^{-1}, 0.444 g, 0.044 mmol, 1 equiv) was dried under vacuum at 110 °C for 12 h before being dissolved in anhydrous THF (20 mL, $[AEC]_0$ = 1 M). AEC (4.0 g, 20 mmol, 450 equiv) and *t*-Bu-P_2 (100 μL, 0.20 mmol, 4.5 equiv., ∼2 M in THF) were then added and the reaction stirred at room temperature (RT). After 21 h at 85% AEC conversion, the catalyst was quenched with acetic acid (∼0.46 mL, 8.0 mmol, 40 equiv. relative to catalyst) and the solution poured into cold hexane (250 mL) to precipitate PAEC-*b*-PEO-*b*-PAEC (L10 vinyl precursor) as a white solid (2.42 g, 63% yield).

2.2. Thiol−Ene Functionalization

E.g., the S20 vinyl precursor (2.08 g, 8.72 mmol [C═C], 1 equiv. [C═C]) was dissolved in degassed acetonitrile (ACN, ∼10 wt %, 20.7 mL) before mercaptosuccinic acid (MSA; 2.62 g, 17.4 mmol, 2 equiv. relative to [C═C]) and 2,2-dimethoxy-2-phenylacetophenone (DMPA; 447 mg, 1.74 mmol, 0.2 equiv. relative to [C═C]) were added. The solution was stirred for 1 h under UV irradiation (365 nm). After decanting off the ACN, the precipitate was washed with diethyl ether (×3) to remove excess MSA before drying under vacuum for >24 h to afford a sticky colorless residue (3.31 g, 98% yield). Full functionalization was confirmed by ^1H NMR spectroscopy (Figure S12).

2.3. Lithium Borate Formation

In an inert atmosphere, e.g., the GB20 acid-functionalized precursor (4.22 g, 12.0 mmol, 2 equiv. MSA) was dissolved in anhydrous DMSO (∼10 wt %, 62 mL) before $B(OH)_3$ (560 mg, 9.03 mmol, 1.5 equiv. relative to MSA) and Li_2CO_3 (334 mg, 4.52 mmol, 0.75 equiv. relative to MSA) were added. The solution was stirred at 60 °C for 12 h after which it was cooled to RT and the polymer isolated by precipitation into diethyl ether (∼300 mL), washing with diethyl ether (×3) and then ACN (×3) to remove residual catalyst and photoinitiator before drying under vacuum for ≥72 h (3.97 g, 82% yield). Borate formation was confirmed by ^1H, ^7Li and $^{11}B\{^1H\}$ NMR and FTIR spectroscopy (Figure S12; Table S1 for all architectures).

2.4. Characterization

Characterization data and techniques are provided in the Supporting Information.

2.5. Cell Fabrication

Polymer binders were cryogenically ball-milled to form powders (Figure S3). Cathode composites were then immediately prepared by mixing single-crystalline NMC811, Li_6PS_5Cl (LPSCl), carbon nanofibers (CNF), and polymer binder in 70:23:2:5 wt % ratio using a mortar and pestle in an argon glovebox. Solid-state cells were assembled in custom PEEK molds by cold pressing (400 MPa) three layers: cathode composite, LPSCl separator, and anode composite ($Li_4Ti_5O_{12}$:LPSCl:CNF, 30:60:10 wt %), with stainless steel current

https://doi.org/10.1021/acsapm.5c04494
ACS Appl. Polym. Mater. 2026, 8, 5459−5470

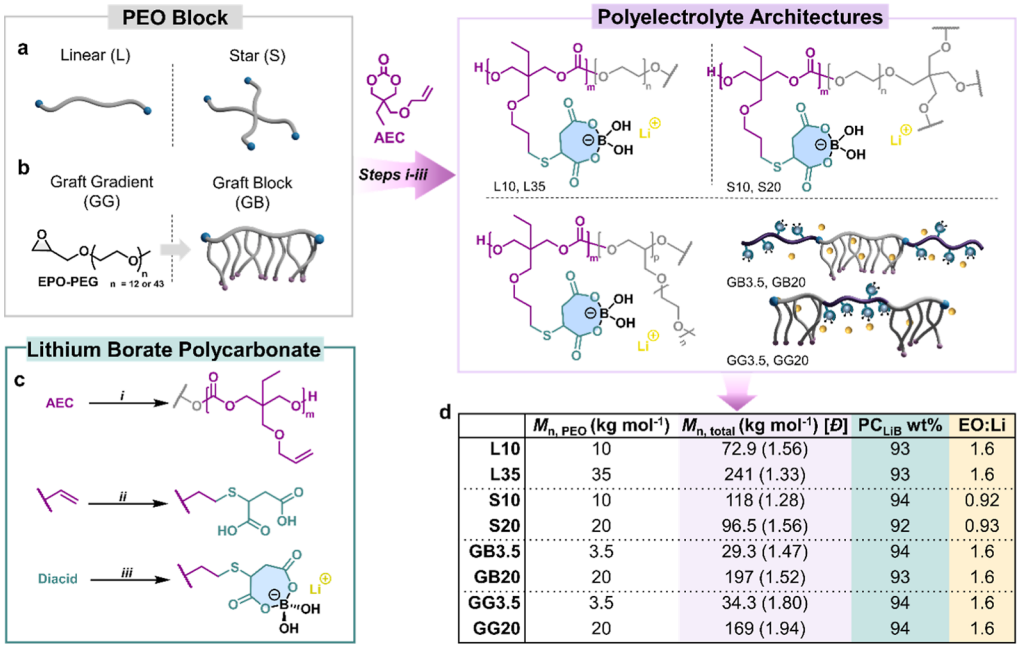

	$M_{n,PEO}$ (kg mol^{-1})	$M_{n,total}$ (kg mol^{-1}) [$Đ$]	PC_{LiB} wt%	EO:Li
L10	10	72.9 (1.56)	93	1.6
L35	35	241 (1.33)	93	1.6
S10	10	118 (1.28)	94	0.92
S20	20	96.5 (1.56)	92	0.93
GB3.5	3.5	29.3 (1.47)	94	1.6
GB20	20	197 (1.52)	93	1.6
GG3.5	3.5	34.3 (1.80)	94	1.6
GG20	20	169 (1.94)	94	1.6

Figure 1. Synthesis and characterization data of architectural polyelectrolyte library. (a) Linear and star poly(EO-*b*-AEC) from PEO macroinitiators (M_n = 10−35 kg mol^{-1}). (b) Graft architectures via sequential (graft block, GB) or one-pot (graft gradient, GG) copolymerization of PEG-epoxide (660 or 2000 g mol^{-1}) with AEC. (c) Synthetic route: *i* = AEC ROP in toluene/THF at 25−60 °C using *t*-Bu-P_2 (linear/star) or *t*-Bu-P_4 (graft) catalysts (see Supporting Information); ii = thiol−ene functionalization with 2-mercapatosuccinic acid under UV irradiation (DMPA photoinitiator, ACN, 2h); iii = lithium boration with $B(OH)_3/Li_2CO_3$ in DMSO (60 °C; 12 h). (d) Polymer library: $M_{n,SEC}$ (THF eluent) and lithium borate polycarbonate content (wt % PC_{LiB} from ^{1}H NMR).

collectors. Cells were cycled at 60 °C under 1 MPa stack pressure. Galvanostatic cycling was performed at 1.75 mA cm^{-2} for at least 100 cycles.

3. RESULTS AND DISCUSSION

3.1. Synthesis of Linear, Star, and Graft Polyelectrolytes

Lithium borate poly(carbonate-*block*-ethers) with different architectures yielded ionically conductive, adhesive, networked binder structures. The synthetic strategy targeted lithium borate polycarbonate contents of 90 wt % with PEO comprising the remaining 10 wt %, based on previous optimization studies with linear systems.[26] Two approaches were developed: a macroinitiator strategy for linear (L) and star (S) architectures and a graft-through method for graft block (GB) and reverse-sequence graft gradient (GG) topologies. GB polymers position PEO segments in the midblock with outer polycarbonate blocks, while GG polymers feature the reverse arrangement with a polycarbonate-rich center transitioning to PEO-rich outer regions. Variation of molar mass (M_n) within each architectural family enabled generation of conductivity-matched pairs with distinct mechanical properties, targeting ionic conductivities of 10^{-4} S cm^{-1} at 60 °C while varying viscoelastic character. This approach prioritized matching key properties across architectures rather than molar mass, enabling investigation of structure-property-performance relationships.

Linear and star architectures were prepared using difunctional or tetra-functional 4-arm PEO macroinitiators (Figure 1a). A linear PEO macroinitiator of M_n 35 kg mol^{-1} (L35) was selected based on optimal values from prior battery studies,[26,29] with 10 kg mol^{-1} (L10) and later 20 kg mol^{-1} variants providing comparisons between architectural families. Star structures (S10, S20) utilized commercial 10 and 20 kg mol^{-1} 4-arm PEO macroinitiators, with each arm contributing around 2.5 or 5 kg mol^{-1}, respectively. Ring-opening polymerization (ROP) of 2-allyloxymethyl-2-ethyltrimethylene carbonate (AEC) (∼1 M in dry THF or toluene) was initiated from these macroinitiators using P_2-*t*-Bu phosphazene base, achieving equilibrium conversions of 80−85%, and yielding poly(ethylene oxide-*block*-2-allyloxymethyl-2-ethyltrimethylene carbonate), poly(EO-*b*-AEC) structures. ^{1}H NMR spectroscopy ($CDCl_3$) confirmed polycarbonate contents of 87−89 wt %, closely matching the target range and corresponding to 92−94 wt % after conversion to the final lithium borate polyelectrolytes (Figure S5 and Table S2). Characterization by size exclusion chromatography (SEC) confirmed monomodal molar masses with dispersities ($Đ$) of 1.3−1.6 and hydroxyl end-group tests further supported successful block formation (Figures S6 and S7). The resulting Li/EO molar ratios were calculated at ∼1.5−1.6 for linear (L10, L35) and ∼0.92−0.93 for star architectures (S10, S20).

For graft architectures, ROP of methoxy-polyethylene glycol epoxide (EPO-PEG) monomers (43−45 or 12−15 ethylene oxide repeat units) enabled control over PEG side-chain length (Figure 1b). Graft block copolymers (GB3.5, GB20) were synthesized by sequential monomer addition: first polymerizing the respective EPO-PEG monomer with the more basic *t*-Bu-P_4 organocatalyst to form the graft bottlebrush PEO midblock followed by AEC addition to grow outer polycarbonate blocks (Figure S8). The nomenclature reflects the total PEO molar mass (3.5 and 20 kg mol^{-1}) in the final isolated polymer, targeted to achieve comparable Li/EO molar ratios (∼1.6) between architectures. In contrast, for reverse-sequence graft gradient copolymers (GG3.5, GG20), one-pot copolymerization of EPO-PEG with AEC monomers yielded polymers with a polycarbonate-rich center transitioning to PEO-rich outer regions, as determined through reactivity ratio

https://doi.org/10.1021/acsapm.5c04494
ACS Appl. Polym. Mater. 2026, 8, 5459−5470

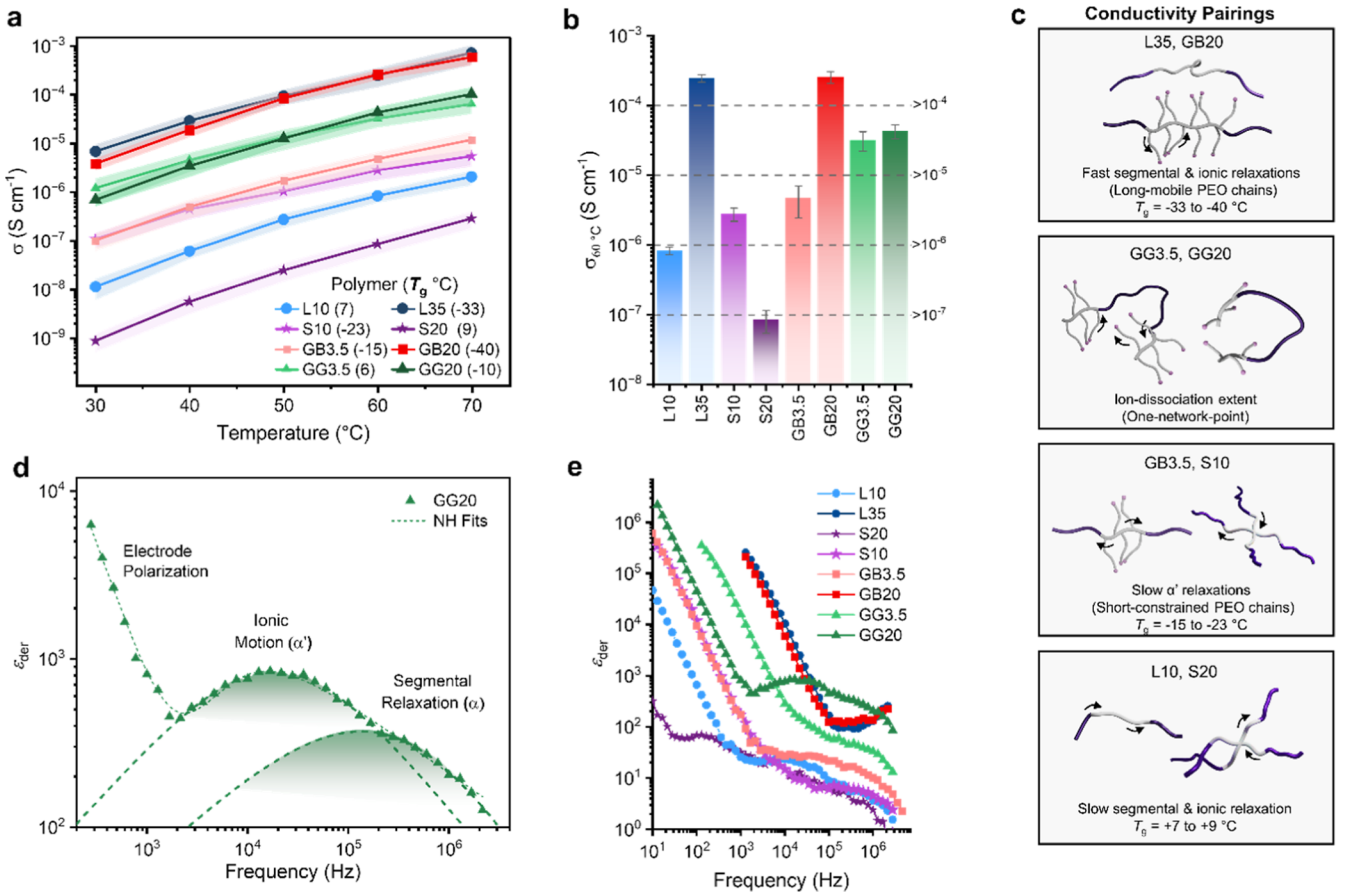

Figure 2. (a) Li-ion conductivities (σ) with temperature (T_g values from DSC); shading represents standard error of $N = 3$ measurements. (b) Conductivity groupings at 60 °C. (c) Schematic illustration of architectural pairings; arrows indicate proposed Li-ion hopping within PEO chains (gray) and lithium borate pendant groups (purple, borate omitted for clarity). (d) Derivative dielectric relaxation (ε_{der}) spectra at 60 °C showing Negami-Havriliak (NH)-fitted segmental α- and α'-relaxation processes and (e) comparing all architectures. Peak heights are considered to generally correlate with ion dissociation capability in these tethered-anion polyelectrolytes.

studies (Figure S9). SEC analysis confirmed controlled polymerization with monomodal distributions and $Đ$ of 1.5−1.9 for all graft structures (Figure S10). These are consistently slightly broader than the linear and star architectures and attributed to the dispersity of the PEO side-chain of the macromonomer and known challenges in SEC analysis of graft polymers.

All polymer precursors underwent postpolymerization modification to introduce lithium borate single-ion conductive sites (Figure 1c). Pendant vinyl groups of the polycarbonate segments were functionalized via UV-initiated thiol−ene reactions with 2-mercaptosuccinic acid, achieving >98% conversion by ^{1}H NMR spectroscopy (loss of vinyl protons at 5.82 and 5.18 ppm in DMSO-d_6). The resulting dicarboxylic acid-functionalized polymers were converted to monochelate lithium borates through reaction with boric acid and lithium carbonate. ^{7}Li and ^{11}B{^{1}H} NMR spectroscopy confirmed characteristic Li (−0.98 ppm) and tetrahedral borate (1.42 ppm) environments, with a minor trigonal boron species (~20.6 ppm) also observed. The stoichiometry of Li_2CO_3 (0.75 equiv.) and $B(OH)_3$ (1.5 equiv.) relative to pendant diacid groups (2 equiv.) was optimized to maximize the tetrahedral borate content (>95%) observed. Complete conversion of the diacid-functionality was supported by both ^{1}H NMR spectroscopy (DMSO-d_6), which showed loss of the carboxylic acid protons at 12.5 ppm and FTIR spectroscopy confirming disappearance of the broad O−H stretches around 3200 cm^{-1} (Figure S12). All final polyelectrolytes were isolated and purified (to remove residual catalyst and photoinitiator) by precipitation (into diethyl ether) and multiple washings (with acetonitrile), then dried under vacuum (>10^{-3} mbar, 60 °C) until constant mass (ca. 48−72 h) and stored under argon (in a glovebox <0.1 ppm of H_2O).

Thermogravimetric analysis (TGA) showed thermal degradation onsets of 122−165 °C, generally following the expected correlation between M_n and thermal stability (Figure S17). The degradation profiles exhibited three steps: the first was attributed to decomposition of the pendant borate and side chain functionality with some competing decarboxylation; the second to evolution of CO_2 (supported by TGA-FTIR analysis, Figure S18); and the third to degradation of the remaining polymer backbone. The polyelectrolytes exhibited lower thermal stability than their diacid precursors (Figure S19), consistent with the lability of the borate coordination. The resulting library of architecturally diverse polyelectrolytes (Figure 1d) with consistent lithium borate polycarbonate content (92−94 wt %) and Li/EO ratios (0.9−1.6) was hot-pressed into standalone films for evaluation of ionic conductivity as the first key binder property.

3.2. Lithium-Ion Conductivity

Temperature-dependent electrochemical impedance spectroscopy (EIS) of these films (ca. 0.9 mm thick, gold blocking

https://doi.org/10.1021/acsapm.5c04494
ACS Appl. Polym. Mater. 2026, 8, 5459−5470

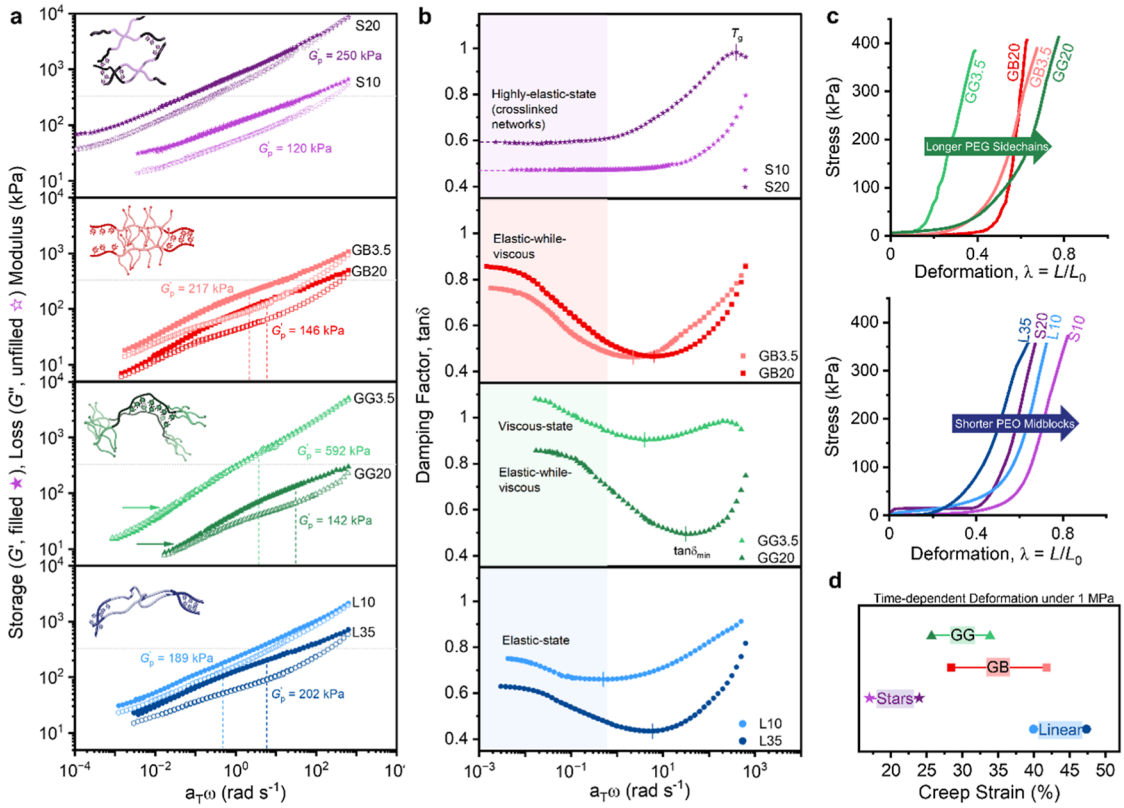

Figure 3. (a) Elastic (G') and viscous (G'') frequency (ω)-dependent moduli TTS master curves at 60 °C. Plateau moduli (G'_p) determined at tanδ minima (as shown). Horizontal lines show Dahlquist criterion for pressure-sensitive adhesives (G' < 330 kPa). G'/G'' crossovers (arrows) observed only for GG architectures. Inset; illustrations of polymer networking interactions. (b) Damping factor (tanδ) highlighting low frequency differences. (c) Compressive stress−strain behavior. (d) Creep resistance at battery cycling conditions (60 °C, 1 MPa).

electrodes, 100 N applied pressure) revealed ionic conductivities spanning 3 orders of magnitude (10^{-4} to 10^{-7} S cm^{-1} at 60 °C). Within each architectural family, lower glass transition temperatures (T_g's) consistently corresponded to enhanced ionic conductivity: L35 > L10, S10 > S20, GB20 > GB3.5, and GG20 > GG3.5, demonstrating the well-established coupling between polymer segmental motion and ion transport (Figure 2a). DSC revealed single T_g values for all polymers, suggesting block miscibility, with GB20 additionally exhibiting a minor melting transition at 37 °C from PEO crystallization (Figure S20). Vogel−Tammann−Fulcher (VTF) analysis of the temperature-dependence of the conductivity data confirmed this role of T_g, with fitted Vogel temperatures (T_0) consistently approximating T_g −50 K (Figures S21−S24). However, when selecting binders based on ionic conductivity (i.e., across architectures), T_g provided only a general trend.

Ranking polymers by conductivity values at 60 °C reveals four distinct groupings: GB20−L35 > GG20−GG3.5 > GB3.5−S10 > L10−S20 (Figure 2b,c). Notably, polymers within each conductivity grouping possess different T_g values and architectures. In the highest conductivity regime (~10^{-4} S cm^{-1}), GB20 and L35 exhibit the lowest T_g values (−40 and −33 °C respectively), consistent with Fox equation predictions for noninteracting miscible blocks (Figure S20). The remaining polymers' higher T_g values are attributed to ionomer-PEO interactions that restrict backbone mobility as reported by Colby and co-workers.[65] In contrast, GG20 (T_g = +6 °C) and GG3.5 (T_g = −10 °C) achieve similar conductivities (~10^{-5} S cm^{-1}) despite a 16 °C difference, while GB3.5 and S10 group together (≤10^{-6} S cm^{-1}) despite GB3.5 (−15 °C) having a more favorable T_g than even the more conductive GG system, highlighting the impact of block sequence.

Consistent with the single T_g observations, small-angle X-ray scattering (SAXS) measurements provided no evidence of block microphase separation while wide-angle X-ray scattering (WAXS) revealed subtle variations in ion aggregate spacing that correlate with these conductivity groupings (2.4−2.6 nm, Figure S25). Importantly, these conductivity-matched pairs provide a framework for investigating how polymer binder mechanical responses, rather than ion transport alone influence composite cathode performance.

Dielectric relaxation spectroscopy (DRS) helped probe the underlying reasons different architectures achieve similar bulk conductivities. Analysis of the derivative dielectric constant (ε_{der}, see Supporting Information for details) revealed two characteristic relaxation processes: a high-frequency α-relaxation attributed to polymer segmental motion and an intermediate-frequency peak related to backbone reorganization during ion motion (Figures 2d and S26).[66] The most conductive polymers (GB20, L35) exhibit minimal separation between segmental and ionic relaxations with elevated dielectric permittivity, indicating fast, coupled dynamics that promote ion dissociation (Figure 2e). Sufficiently high PEO M_n in these polymers, either as a linear midblock (L35) or long side chains (GB20), appears critical for this efficient transport.[67] The intermediate regime (~10^{-5} S cm^{-1}) showed GG20 and GG3.5 with more distinct peak separation (fitted to Negami-Havriliak functions), suggesting that PEO segments unconstrained at both ends maintain comparable ion transport

https://doi.org/10.1021/acsapm.5c04494
ACS Appl. Polym. Mater. 2026, 8, 5459−5470

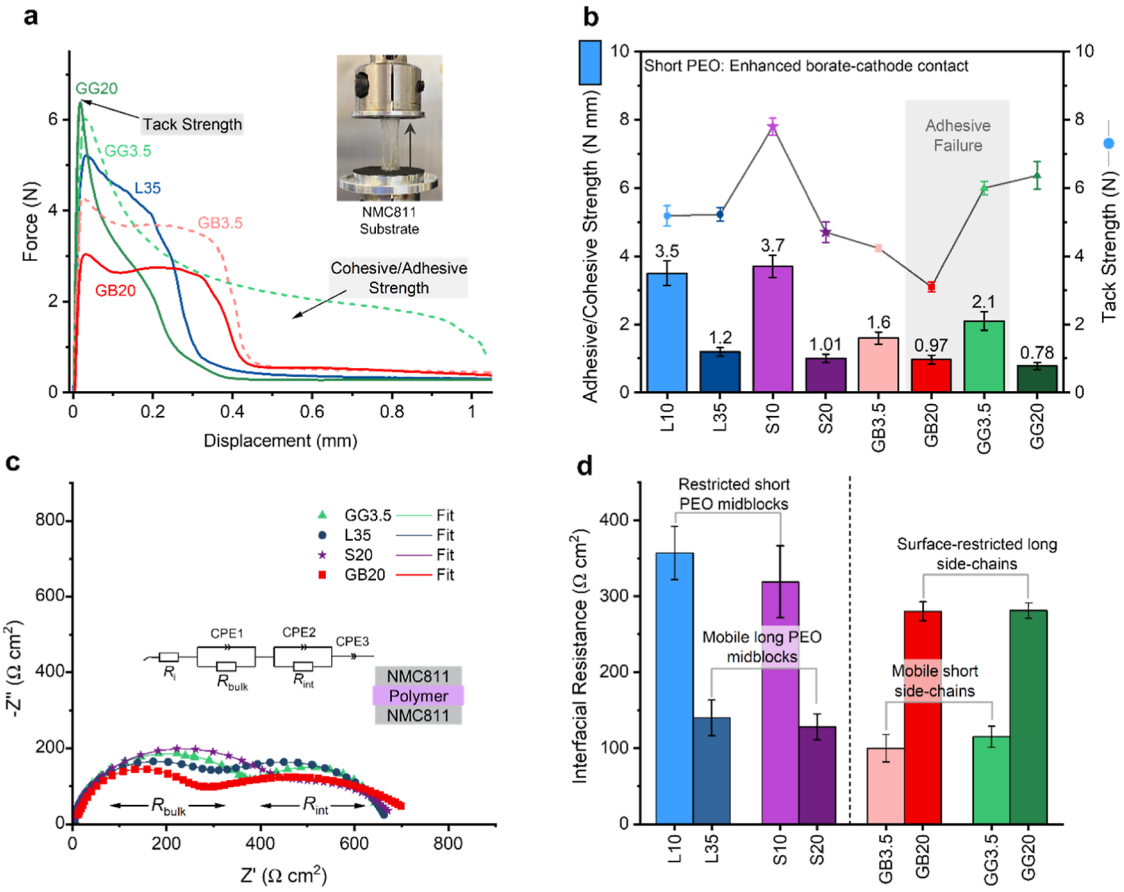

Figure 4. (a) Adhesion tests against NMC811 (60 °C, 1 MPa load): force−displacement curves showing characteristic profiles for different architectures; inset photo of S20 testing. (b) Corresponding tack strength and cohesive/adhesive strength; gray region indicates failure mode. (c) Representative Nyquist curves with equivalent circuit fitting for bulk polymer (R_{bulk}) and interfacial resistance (R_{int}). (d) R_{int} values for all polymer architectures, indicating relationship to PEO midblock and side-chain lengths. Error bars represent standard deviation of $N = 3$ samples.

dynamics regardless of M_n.[68−70] Lower conductivity pairs display progressively slower ionic motion (time scales approaching 10^{-4} s) with similarities between GB3.5 and S10 attributed to their comparable PEO content (3.5 kg mol^{-1} total in GB3.5 versus ∼2.5 kg mol^{-1} per arm in S10) creating equivalent energetic environments. The lowest conductivity systems (S20, L10) show dramatically restricted dynamics, with S20's four ionic network points and central covalent linker likely contributing to the slowest transport.

Transference numbers (t_{Li+} = 0.84−0.96) estimated via the Bruce-Vincent method approach unity as expected for single-ion conductors with slightly lower values at decreasing molar mass attributed to increased mobility of shorter chain systems (Figure S27). To validate these conductivity findings in battery environments, ion transport was investigated in polymer-Li_6PS_5Cl composites (23:5 weight ratio) that mirror the cathode compositions (Figure S28). These composites exhibited slightly enhanced ionic conductivities compared to the neat polymers while maintaining the same architectural hierarchy (GB20 ∼ L35 > GG20 ∼ GG3.5 > GB3.5 ∼ S10 > L10 ∼ S20), confirming that bulk polymer relationships remain valid in composite systems with sulfide electrolytes.

3.3. Architecture-Dependent Mechanical Properties

Polymer binder mechanical properties serve dual functions: enabling composite formation during processing and maintaining integrity during cycling. Oscillatory rheology was employed to investigate the viscoelastic signatures correlating with polymer architecture for these polyelectrolytes. Time−temperature superposition (TTS) was applied to extend the accessible frequency range and thus time scales over which the behavior could be observed with master curves generated at 60 °C. The temperature-dependence of shift factors (a_T) was fitted to the Williams−Landel−Ferry (WLF) equation, and Gurp−Palmen plots used to further validate the thermo-rheological behavior (Figures S29 and S30). Storage moduli (G') exceeded loss moduli (G'') across most frequencies, indicating solid-like binder behavior, except for GG polymers which exhibited G'/G'' crossovers at low frequencies (Figure 3a). This distinctive flow character stems from GG architectures having only one effective polycarbonate ionic network point per chain compared to two for GB and linear architectures, and four for star architectures. Plateau moduli (G_p', measured at the minimum in tanδ) ranged from 120 to 592 kPa across architectures (Figure S31), with higher values at increased molar mass (L35 > L10, S20 > S10) and shorter side chains (GB3.5 > GB20, GG3.5 > GG20) consistent with established enhanced chain entanglement effects.[50]

The damping factor (tanδ = G''/G') measures how effectively materials absorb and redistribute mechanical stress. It varied markedly across architectures particularly at lower frequencies relating to longer-term viscoelastic response expected to be more relevant to battery cycling time scales (Figure 3b). Star polymers showed flat, low tanδ values (∼0.4−0.6) indicating highly elastic behavior with limited

https://doi.org/10.1021/acsapm.5c04494
ACS Appl. Polym. Mater. 2026, 8, 5459−5470

energy dissipation. GB20 and L10 achieved intermediate values (~0.8), effectively balancing elastic and viscous responses through temporary chain disentanglement. Graft-gradient structures exhibited the highest tanδ values (>0.8−1.0), correlating with their viscous flow behavior and suggesting the possibility for superior stress redistribution capabilities for accommodating cycling-induced stresses.

Having established these mechanical signatures for architectures, attention returns to the conductivity-matched pairs to evaluate how mechanical properties differ as a result. Among the high-conductivity polymers (~10^{-4} S cm^{-1}), GB20 and L35 demonstrated distinct mechanical responses: GB20 exhibited lower plateau modulus (146 vs 202 kPa) but superior creep resistance (28% vs 47% strain under 1 MPa at 60 °C, Figure 3d) and in stress−strain measurements, pronounced strain-stiffening (Figure 3c, upturn at 42% strain, 39.2 MPa stiffening modulus vs 16%, 12.5 MPa for L35), attributed to steric repulsion from extended side chains. The intermediate-conductivity GG20 and GG3.5 pair (~10^{-5} S cm^{-1}) illustrated molar mass effects, with GG3.5 showing the highest G'_p (592 kPa) and fastest relaxation (56 s vs 360 s for GG20), yet both maintaining high damping factors. Notably, GB3.5 and L35 demonstrated similar plateau moduli (217 vs 202 kPa) and tanδ profiles despite different conductivities, enabling evaluation of how mechanical properties might compensate for reduced ion transport. Star polymers exhibited good dimensional stability (17−24% creep strain) but low damping capacity, while linear polymers showed higher creep (40−50%) with moderate damping, suggesting different strategies for potentially managing battery cycling stresses.

3.4. Interfacial Adhesion and Electrochemical Properties

Beyond bulk mechanical response, polymer-cathode interfacial interactions are critical for composite integrity and electrochemical performance. The viscoelastic properties established above also relate to adhesive behavior: all architectures meet the Dahlquist criterion for pressure-sensitive adhesives (G' < 330 kPa at 0.628 rad s^{-1}, Figure 3a), enabling interfacial bonding under applied load during battery assembly and operation while remaining nontacky at ambient conditions. While composite cathodes contain multiple interfaces (binder-NMC811, binder-LPSCl, binder-carbon), NMC811 represents the bulk component (70 wt %), making polymer-NMC811 interactions particularly important. Binder−LPSCl interactions were explored above through conductivity measurements in composites; here, tack tests directly probe polymer-NMC811 interfacial adhesion at battery-relevant conditions (60 °C, 1 MPa applied pressure).

These tests provided two metrics (Figure 4a): tack strength (maximum separation force), which reflects the ability to form immediate bonds under pressure, and adhesive/cohesive strength (debonding energy or total separation work), indicating interfacial interaction strength under sustained load. Tack strength ranged from <4 N (GB20) to 7.8 N (S10), with S10 and the GG architectures (6−6.5 N) showing notably higher values that may complicate uniform distribution during dry mixing. Adhesive/cohesive strength showed a consistent inverse molar mass trend: shorter chains produced higher values across all architecture types (L10 ≫ L35, S10 ≫ S20, GB3.5 > GB20, GG3.5 > GG20). Although higher M_n would typically enhance cohesive strength, this trend indicates that debonding is dominated by interfacial lithium borate-NMC811 interactions rather than bulk cohesion, with shorter chains enabling greater borate accessibility to the cathode surface. This is consistent with failure mode observations: most architectures failed cohesively with visible strand formation, supporting strong interfacial adhesion via borate−cathode interactions. Within conductivity-matched pairs, L35 and GB20 showed similar adhesive/cohesive strength (0.97−1.2 N mm), while S10 outperformed GB3.5 (roughly double), L10 surpassed S20 (>3 times), and GG3.5 exceeded GG20 (roughly double).

Interfacial resistance measurements against NMC811 cathodes revealed that ion transfer at the interface followed trends distinct from bulk conductivity and adhesive/cohesive strength (Figure 4c,d). These trends were reproducible and systematic within each architectural family. Whereas adhesion is governed by borate group accessibility, interfacial resistance (R_{int}, from symmetric NMC|polyelectrolyte|NMC cells) is attributed primarily to PEO segmental mobility at the cathode surface. For linear and star architectures, the opposite trend to adhesion was observed: lower R_{int} with longer PEO (L35/S20:128−140 Ω·cm^2 vs > 319 Ω·cm^2 for L10/S10). This is attributed to longer chains between borate anchor points preserving more PEO segmental mobility to aid ion transfer. For graft architectures, R_{int} followed the same trend as adhesion: shorter PEO side chains gave lower R_{int}. While this is consistent with better interfacial contact through stronger adhesion, the R_{int} reduction (nearly 3-fold to ~100 Ω·cm^2 for GB3.5/GG3.5 vs 280 ± 12 Ω·cm^2 for GG20/GB20) was more pronounced than the adhesion difference (roughly 2-fold) alone would account for. Additionally, R_{int} values for GB20/GG20 were comparable to L10/S10 despite the latter showing significantly stronger adhesive character. This suggests that for longer grafted PEO side-chains, surface coordination or steric hindrance at the NMC interface further restricted ion transfer. Across all architectures, these trends highlight that PEO mobility at the cathode surface is a primary determinant of interfacial resistance. Within conductivity-matched pairs, these architecture-dependent R_{int} differences proved critical for subsequent battery performance. All architectures demonstrated adequate oxidative stability (4.31−4.58 V vs Li/Li^+, Figure S35) for testing in full battery cells.

3.5. Property−Performance Relationships in Solid-State Batteries

Having established that conductivity-matched binders exhibit distinct mechanical and interfacial properties, full cell battery testing was conducted to evaluate their contributions to composite cathode performance. Composite cathodes were prepared by cryo-ball milling the polyelectrolyte binders to form fine powders and then hand-grinding them at 5 wt % with sc-NMC811 (70 wt %), LPSCl solid electrolyte (23 wt %), and carbon (2 wt %). This dry-processing approach followed by densification was used to avoid complications due to the solvent incompatibility of LPSCl. Cells were assembled in specialized PEEK cells with $Li_4Ti_5O_{12}$ (LTO) anode, LPSCl solid electrolyte and the composite cathode and cycled at 60 °C under 1 MPa stack pressure at 1.75 mA cm^{-2}. The elevated temperature accentuates chain dynamics differences while eliminating room-temperature crystallinity complications. It also accelerates cell degradation, helping to observe binder performance differences within a reasonable time frame (100 cycles). As the binder ionic conductivity (~10^{-4} S cm^{-1} at 60 °C) is an order of magnitude lower than LPSCl (~10^{-3} S cm^{-1}), binder content was minimized to 5 wt % to preserve the

https://doi.org/10.1021/acsapm.5c04494
ACS Appl. Polym. Mater. 2026, 8, 5459−5470

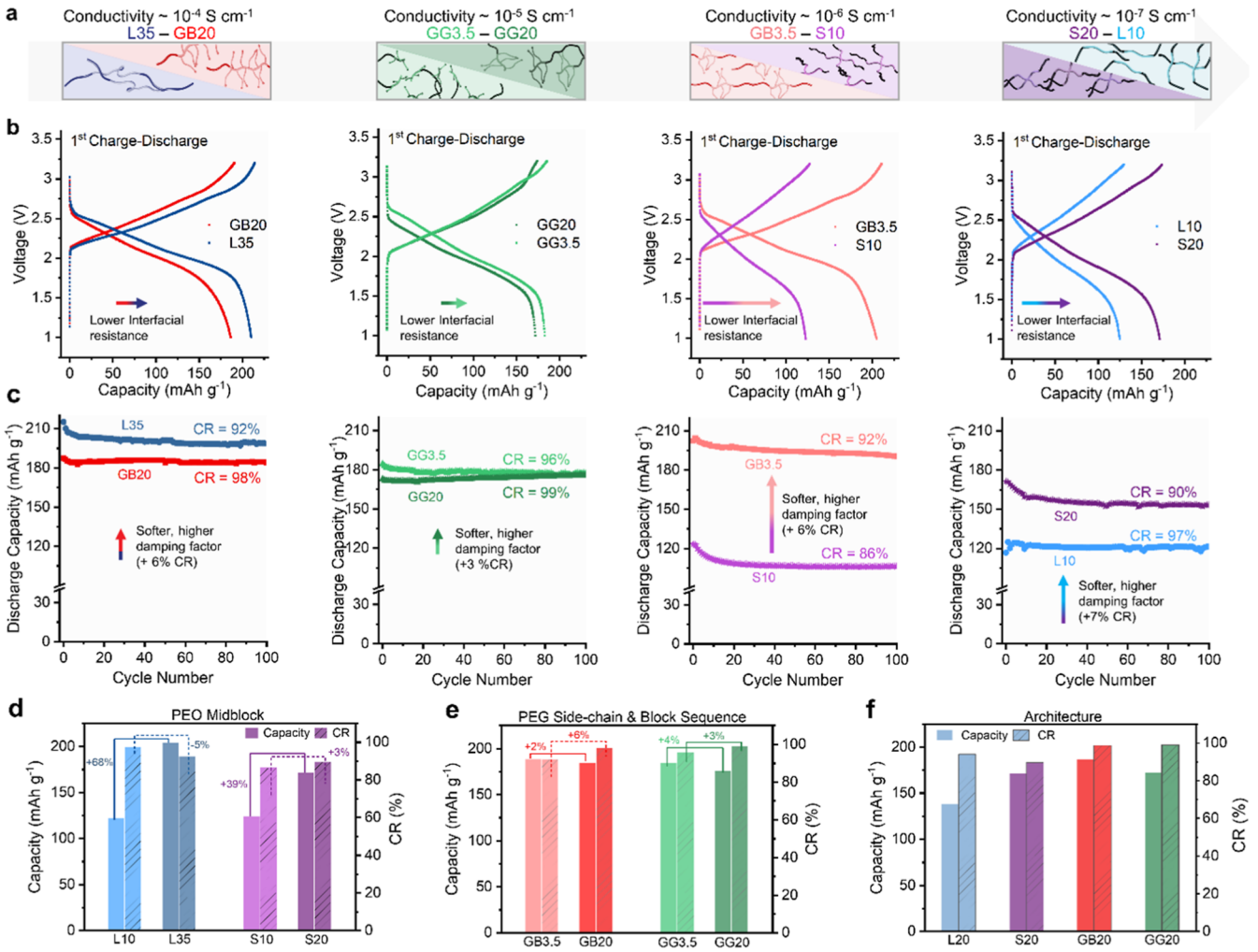

Figure 5. (a) Conductivity pairings. (b) 1st charge−discharge profiles for cells with NMC/LPSCl/C/binder, LPSCl electrolyte and $Li_4Ti_5O_{12}$ (LTO) cycled at 1.75 mA cm^{-2}, 60 °C, 1 MPa stack pressure. (c) Capacity retention (CR) after 100 charge−discharge cycles. (d,e) M_n effects: linear and star PEO midblock; graft PEG side-chain. (f) Architectural hierarchy at equivalent PEO M_n (20 kg mol^{-1}); Conductivity: GB20 > GG20 > L20 > S20.

solid electrolyte percolation network. Lower loadings (1−2 wt %) were found to compromise capacity retention (Figure S37). In contrast, conventional PTFE binders typically function at 0.1−1 wt % loadings, but serve solely a mechanical role without contributing to ion transport.

Initial discharge capacities ranged from 123 to 210 mAh g^{-1} across architectures, compared to 175 mAh g^{-1} for PTFE and 155 mAh g^{-1} with no binder under identical conditions. While polymers with the highest ionic conductivities generally delivered superior capacities, notable exceptions emerged: GB3.5 achieved 205 mAh g^{-1} despite moderate conductivity, and shorter PEG side chains consistently outperformed longer ones (GB3.5 > GB20, GG3.5 > GG20). These trends align more closely with interfacial resistance than bulk ionic conductivity and within conductivity-matched pairs, the binder with lower interfacial resistance consistently delivered higher initial capacity (Figure 5a,b). Thus, L35 achieved the highest capacity (210 mAh g^{-1}) by combining high conductivity with moderate interfacial resistance (125 Ω·cm^2), while GB3.5's unexpectedly strong performance likely stems from its low interfacial resistance (<100 Ω·cm^2). While direct measurement of binder distribution within composites was not possible, all samples were prepared identically using cryo-milled polymer powders and identical mixing protocols to minimize distribution variations. The elevated tack observed for S10 and GG polymers could potentially affect distribution, though the consistency and reproducibility of performance trends suggest systematic property effects dominate. These results demonstrate that interfacial charge transfer, not just bulk conductivity, critically determines initial capacity.

Capacity retention over 100 cycles revealed the influence of mechanical properties on cycling stability (Figure 5c). Among high-conductivity binders (~10^{-4} S cm^{-1}), L35 retained 92% of its initial capacity after 100 cycles, whereas GB20 achieved a superior retention of 98%. For context, PTFE achieved only 84% retention under identical conditions. GB20s enhanced retention over L35 is consistent with its lower creep resistance (28% strain under sustained load vs 47% for L35), balanced viscoelastic response (tanδ ~0.8), and strain-stiffening behavior that likely preserves interfacial contact during volume changes. Indeed, within each conductivity pair, better capacity retention consistently correlated with binders exhibiting softer character (lower G'_p < 200 kPa) and higher damping factor (tanδ>0.7). While polymer mechanical properties may evolve during cycling due to stress accumulation and potential chain degradation, the strong correlation between initial polymer

https://doi.org/10.1021/acsapm.5c04494
ACS Appl. Polym. Mater. 2026, 8, 5459−5470

mechanical signatures and cycling performance suggests these properties are good indicators of cell performance and reasonably resilient to cycling-induced changes. The highest capacity retentions were achieved by graft polymers with long PEO side-chains (GG20, GB20:98−99%), which combine balanced viscoelastic properties (G' ∼140−200 kPa, tanδ ∼0.8). In contrast, star binders exhibited the poorest capacity retentions (86−90%), consistent with their low, flat tanδ values across low frequencies that limit their ability to redistribute cycling-induced stresses (Figure 5d,e).

These results clarify that initial capacity and retention are governed by different property sets. Initial capacity correlates with high ionic conductivity (>10^{-4} S cm^{-1}) and low interfacial resistance (<125 Ω·cm^2), while retention is dominated by softer, lower G' polymers (<200 kPa) with high damping factor (tanδ >0.7). While these relationships might seem intuitive, they were only revealed by comparing conductivity-matched binders where architecture varied mechanical and interfacial properties independently. When comparing binders at equivalent PEO molar mass (20 kg mol^{-1}) where both conductivity and mechanical properties vary simultaneously, such clear structure-property relationships become obscured. At equivalent molar mass, the architectural hierarchy in capacity retention (GB20 > GG20 > L20 > S20) and capacity (GB20 > GG20 > S20 > L20) reflects competing influences of multiple properties rather than isolating individual contributions (Figure 5f). M_n sensitivity also varied across architectures, with linear and star structures showing pronounced dependence (L35 > L20 > L10; S20 > S10) while graft architectures demonstrated greater stability across molar masses (Figure 5d). Since L35 maximizes initial capacity while GB20 optimizes retention, blends of these binders were tested and showed promise and at extended cycling (>200 cycles, Figure S43). This architectural blending approach may enable further optimization of overall cell performance, including at room temperature.

4. CONCLUSIONS

This work investigates how polymer architecture (linear, star and different graft sequences) controls ionic conductivity, rheological mechanical response, and electrochemical interfacial adhesive properties to identify their relative contributions to solid-state battery composite cathode performance. Lithium borate polyelectrolytes with 10 wt % PEO were synthesized via cyclic carbonate ring-opening polymerization followed by postpolymerization installation of the lithium borate to the polycarbonate block. By varying molar mass and side-chain length across architectures, we identified pairs of binders with matched ionic conductivities but fundamentally different mechanical signatures and adhesive profiles.

The binders (5 wt %) were tested in composite cathodes comprising single-crystal NMC811, LPSCl and carbon in full cells with LTO anode and LPSCl solid electrolyte cycled at 60 °C under 1 MPa applied pressure, revealing differences in both initial discharge capacities and capacity retention. Initial discharge capacity was found to correlate with binder ionic conductivity as expected, but polymer-cathode interfacial resistance was also key. Within conductivity-matched binder pairs, lower interfacial resistance consistently resulted in higher capacities, with some binders achieving unexpectedly high performance (up to 210 mAh g^{-1}) despite only moderate bulk conductivity. In contrast, capacity retention was found to depend primarily on the viscoelastic character and damping factor of the binder. Within pairs, binders with softer character (lower G', <200 kPa) and higher damping factor (higher tanδ, >0.7) consistently achieved superior retention. Graft block architectures, particularly GB20 with long PEO side chains (44−45 EO repeat units), proved most effective.

These findings challenge conventional emphasis on solely maximizing binder ionic conductivity and targeting vague elastomeric polymer properties for optimizing composite cathode performance. Designing conductivity matched polymers using architecture to systematically vary mechanical and interfacial properties proves more effective than standard approaches varying only molar mass and composition. While this work establishes architecture property performance relationships at 60 °C in specialized PEEK-cells, future studies will explore whether these findings extend to room temperature operation, commercial pouch cell formats, and sheet type composite cathodes. Beyond composite cathodes, these architectural polymers are expected to open routes to gel and hydrogel electrolytes with enhanced ionic conductivity and built-in mechanical tunability plus could be explored as polymer electrolytes in silicon anode systems that demand compliance under extreme volume changes, as well as other flexible energy storage devices.

■ ASSOCIATED CONTENT

Supporting Information

The Supporting Information is available free of charge at https://pubs.acs.org/doi/10.1021/acsapm.5c04494.

Full materials, instrument techniques and experimental procedures for all architectures; polymer characterization (SEC traces, reactivity ratio calculations,[66, 67] end-group tests,[68] Figures S1−S11); lithium borate formation and NMR characterization (^{1}H, ^{13}C, ^{7}Li, ^{11}B and FTIR, Figures S12−16); thermal analysis (TGA and DSC, Figures S17−S20); ion transport and structural analysis (Nyquist plots, VTF fits, WAXS data, DRS,[65, 69, 70] Figures S21−S26), transference numbers and composite EIS (Figures S27−S28); additional rheology and adhesion data (Figures S29−S33); and electrochemical stability (Figures S34−S36) and extended cell cycling (Figures S37−S43) (PDF)

■ AUTHOR INFORMATION

Corresponding Author

Georgina L. Gregory − *Department of Chemistry, University of Oxford, Chemistry Research Lab, Oxford OX1 3TA, U.K.*; orcid.org/0000-0002-4688-9269; Email: georgina.gregory@chem.ox.ac.uk

Authors

Zoé Lacour − *Department of Chemistry, University of Oxford, Chemistry Research Lab, Oxford OX1 3TA, U.K.*

Kanyapat Yiamsawat − *Department of Chemistry, University of Oxford, Chemistry Research Lab, Oxford OX1 3TA, U.K.*

Complete contact information is available at: https://pubs.acs.org/10.1021/acsapm.5c04494

Author Contributions

Z.L: investigation, data curation, analysis, writing-reviewing; K.Y.: data curation, reviewing-editing; G.G: supervision, resources, writing-reviewing and editing.

https://doi.org/10.1021/acsapm.5c04494
ACS Appl. Polym. Mater. 2026, 8, 5459−5470

Notes

The authors declare no competing financial interest.

■ ACKNOWLEDGMENTS

This work was funded by the Royal Society Dorothy Hodgkin Fellowship (DHF\R1\221101) and Royal Society Enhancement Award (DHF\ERE\221003). The work was supported by the Faraday Institution SOLBAT Project (FIRG026 and FIRG056). K.Y. acknowledges scholarship funding from the Royal Government of Thailand's Development and Promotion of Science and Technology Talents Project (DPST).

■ REFERENCES

(1) Xu, Z.; Dong, Q.; Li, W. Architectural Design of Block Copolymers. *Macromolecules* **2024**, *57* (5), 1869−1884.
(2) Self, J. L.; Zervoudakis, A. J.; Peng, X.; Lenart, W. R.; Macosko, C. W.; Ellison, C. J. Linear, Graft, and Beyond: Multiblock Copolymers as Next-Generation Compatibilizers. *JACS Au* **2022**, *2* (2), 310−321.
(3) Guo, Z.-H.; Le, A. N.; Feng, X.; Choo, Y.; Liu, B.; Wang, D.; Wan, Z.; Gu, Y.; Zhao, J.; Li, V.; et al. Janus Graft Block Copolymers: Design of a Polymer Architecture for Independently Tuned Nanostructures and Polymer Properties. *Angew. Chem., Int. Ed.* **2018**, *57* (28), 8493−8497.
(4) Bakar, R.; Darvishi, S.; Aydemir, U.; Yahşi, U.; Tav, C.; Menceloğlu, Y. Z.; Şenses, E. Decoding Polymer Architecture Effect on Ion Clustering, Chain Dynamics, and Ionic Conductivity in Polymer Electrolytes. *ACS Appl. Energy Mater.* **2023**, *6* (7), 4053−4064.
(5) Xie, K.; Fu, Q.; Chen, F.; Zhu, H.; Wang, X.; Huang, G.; Zhan, H.; Liang, Q.; Doherty, C. M.; Wang, D.; et al. Controlling the Supramolecular Architecture Enables High Lithium Cationic Conductivity and High Electrochemical Stability for Solid Polymer Electrolytes. *Adv. Funct. Mater.* **2024**, *34* (17), 2315495.
(6) Won, G.; Jo, M. S.; Jeong, Y. H.; Seo, S.; Kim, S.; Kwon, D.-S.; Jeong, D.; Shim, J. Discovery of Optimal Interplay between Grafting Ratio and Side-Chain Interval in Adhesive Polymer Binders for Lithium-Ion Batteries. *ACS Appl. Energy Mater.* **2025**, *8* (13), 8907−8913.
(7) Maw, M.; Morgan, B. J.; Dashtimoghadam, E.; Tian, Y.; Bersenev, E. A.; Maryasevskaya, A. V.; Ivanov, D. A.; Matyjaszewski, K.; Dobrynin, A. V.; Sheiko, S. S. Brush Architecture and Network Elasticity: Path to the Design of Mechanically Diverse Elastomers. *Macromolecules* **2022**, *55* (7), 2940−2951.
(8) Liffland, S.; Hillmyer, M. A. Enhanced Mechanical Properties of Aliphatic Polyester Thermoplastic Elastomers through Star Block Architectures. *Macromolecules* **2021**, *54* (20), 9327−9340.
(9) Sulley, G. S.; Poon, K. C.; Gregory, G. L.; Williams, C. K. (AB)n Star Block Polymers Derived from CO2: Influence of Architecture and Postpolymerization Modification. *Macromolecules* **2025**, *58*, 11291.
(10) Lv, M.; Zhao, R.; Hu, Z.; Yang, J.; Han, X.; Wang, Y.; Wu, C.; Bai, Y. Binder design strategies for cathode materials in advanced secondary batteries. *Energy Environ. Sci.* **2024**, *17* (14), 4871−4906.
(11) He, Q.; Ning, J.; Chen, H.; Jiang, Z.; Wang, J.; Chen, D.; Zhao, C.; Liu, Z.; Perepichka, I. F.; Meng, H.; et al. Achievements, challenges, and perspectives in the design of polymer binders for advanced lithium-ion batteries. *Chem. Soc. Rev.* **2024**, *53* (13), 7091−7157.
(12) Mao, C.; Dong, J.; Li, J.; Zhai, X.; Ma, J.; Luan, S.; Shen, X.; Wang, Y.; Zhang, P.; Sun, H.; et al. Toward Practical All-Solid-State Batteries: Current Status of Functional Binders. *Adv. Mater.* **2025**, *37* (16), No. e2500079.
(13) Kim, Y. J.; Hoang, T. D.; Han, S. C.; Bang, J. A.; Kang, H. W.; Kim, J.; Park, H.; Park, J.-H.; Park, J.-W.; Park, G.; et al. Exploring optimal cathode composite design for high-performance all-solid-state batteries. *Energy Storage Mater.* **2024**, *71*, 103607.
(14) Bielefeld, A.; Weber, D. A.; Janek, J. Modeling Effective Ionic Conductivity and Binder Influence in Composite Cathodes for All-Solid-State Batteries. *ACS Appl. Mater. Interfaces* **2020**, *12* (11), 12821−12833.
(15) Stakem, K. G.; Leslie, F. J.; Gregory, G. L. Polymer Design for Solid-State Batteries and Wearable Electronics. *Chem. Sci.* **2024**, *15* (27), 10281−10307.
(16) Janek, J.; Zeier, W. G. Challenges in speeding up solid-state battery development. *Nat. Energy* **2023**, *8* (3), 230−240.
(17) Li, C.; Nie, S.; Li, H. Towards Efficient Polymeric Binders for Transition Metal Oxides-based Li-ion Battery Cathodes. *Chem.−Eur. J.* **2024**, *30* (16), No. e202303733.
(18) Chen, X.; Qiu, S.; Jian, Z.; Hu, Y.; Chen, D.; Lu, Z.; Liu, C. Designing a Self-Extinguishing System in a Composite Electrolyte for Highly Safe Solid-State Lithium Metal Batteries. *ACS Nano* **2025**, *19* (20), 19297−19309.
(19) Lu, Y.; Zhao, C.-Z.; Yuan, H.; Hu, J.-K.; Huang, J.-Q.; Zhang, Q. Dry electrode technology, the rising star in solid-state battery industrialization. *Matter* **2022**, *5* (3), 876−898.
(20) Kim, N.-Y.; Kim, J.-H.; Koo, H.; Oh, J.; Pang, J.-H.; Kang, K.-D.; Chae, S.-S.; Lim, J.; Nam, K. W.; Lee, S.-Y. Material Challenges Facing Scalable Dry-Processable Battery Electrodes. *ACS Energy Lett.* **2024**, *9* (11), 5688−5703.
(21) Chen, B.; Zhang, Z.; Xiao, M.; Wang, S.; Huang, S.; Han, D.; Meng, Y. Polymeric Binders Used in Lithium Ion Batteries: Actualities, Strategies and Trends. *ChemElectroChem* **2024**, *11* (14), No. e202300651.
(22) Hong, S.-B.; Lee, Y.-J.; Kim, U.-H.; Bak, C.; Lee, Y. M.; Cho, W.; Hah, H. J.; Sun, Y.-K.; Kim, D.-W. All-Solid-State Lithium Batteries: Li+-Conducting Ionomer Binder for Dry-Processed Composite Cathodes. *ACS Energy Lett.* **2022**, *7* (3), 1092−1100.
(23) Ye, W.; He, W.; Long, J.; Chen, P.; Ding, B.; Dou, H.; Zhang, X. Versatile Composite Binder with Fast Lithium-Ion Transport for LiCoO2 Cathodes. *ACS Appl. Mater. Interfaces* **2024**, *16* (14), 17401−17410.
(24) Cha, J.; Kim, S.; Nakate, U. T.; Kim, D.-W. Highly conductive composite cathode prepared by dry process using Nafion-Li ionomer for sulfide-based all-solid-state lithium batteries. *J. Power Sources* **2024**, *613*, 234914.
(25) Oh, J.; Choi, S. H.; Chang, B.; Lee, J.; Lee, T.; Lee, N.; Kim, H.; Kim, Y.; Im, G.; Lee, S.; et al. Elastic Binder for High-Performance Sulfide-Based All-Solid-State Batteries. *ACS Energy Lett.* **2022**, *7* (4), 1374−1382.
(26) Charlesworth, T.; Yiamsawat, K.; Gao, H.; Rees, G. J.; Williams, C. K.; Bruce, P. G.; Pasta, M.; Gregory, G. L. Lithium Borate Polycarbonates for High-Capacity Solid-State Composite Cathodes. *Angew. Chem., Int. Ed.* **2024**, *63* (33), No. e202408246.
(27) Lee, K.; Lee, J.; Choi, S.; Char, K.; Choi, J. W. Thiol−Ene Click Reaction for Fine Polarity Tuning of Polymeric Binders in Solution-Processed All-Solid-State Batteries. *ACS Energy Lett.* **2019**, *4* (1), 94−101.
(28) Lee, J.; Lee, K.; Lee, T.; Kim, H.; Kim, K.; Cho, W.; Coskun, A.; Char, K.; Choi, J. W. In Situ Deprotection of Polymeric Binders for Solution-Processible Sulfide-Based All-Solid-State Batteries. *Adv. Mater.* **2020**, *32* (37), 2001702.
(29) Gregory, G. L.; Gao, H.; Liu, B.; Gao, X.; Rees, G. J.; Pasta, M.; Bruce, P. G.; Williams, C. K. Buffering Volume Change in Solid-State Battery Composite Cathodes with CO2-Derived Block Polycarbonate Ethers. *J. Am. Chem. Soc.* **2022**, *144* (38), 17477−17486.
(30) Yeo, H.; Gregory, G. L.; Gao, H.; Yiamsawat, K.; Rees, G. J.; McGuire, T.; Pasta, M.; Bruce, P. G.; Williams, C. K. Alternatives to fluorinated binders: recyclable copolyester/carbonate electrolytes for high-capacity solid composite cathodes. *Chem. Sci.* **2024**, *15* (7), 2371−2379.
(31) Shen, C.; Zhao, Q.; Shan, N.; Jing, B. B.; Evans, C. M. Conductivity−modulus− relationships in solvent-free, single lithium ion conducting network electrolytes. *J. Polym. Sci.* **2020**, *58* (17), 2376−2388.

https://doi.org/10.1021/acsapm.5c04494
ACS Appl. Polym. Mater. 2026, 8, 5459−5470

(32) Zhou, K.; Lu, S.; Mish, C.; Chen, Y.-T.; Feng, S.; Kim, J.; Song, M.-S.; Kim, H. A.; Liu, P. Tailored Cathode Composite Microstructure Enables Long Cycle Life at Low Pressure for All-Solid-State Batteries. *ACS Energy Lett.* **2025**, *10* (2), 966−974.
(33) Naik, K. G.; Jangid, M. K.; Vishnugopi, B. S.; Dasgupta, N. P.; Mukherjee, P. P. Interrogating the Role of Stack Pressure in Transport-Reaction Interaction in the Solid-State Battery Cathode. *Adv. Energy Mater.* **2025**, *15* (10), 2403360.
(34) Gao, X.; Liu, B.; Hu, B.; Ning, Z.; Jolly, D. S.; Zhang, S.; Perera, J.; Bu, J.; Liu, J.; Doerrer, C.; et al. Solid-state lithium battery cathodes operating at low pressures. *Joule* **2022**, *6* (3), 636−646.
(35) Miao, X.; Guan, S.; Ma, C.; Li, L.; Nan, C.-W. Role of Interfaces in Solid-State Batteries. *Adv. Mater.* **2023**, *35* (50), 2206402.
(36) Cao, Z.; Yao, X.; Park, S.; Deng, K.; Zhang, C.; Chen, L.; Fu, K. Enhancing cathode composites with conductive alignment synergy for solid-state batteries. *Sci. Adv.* **2025**, *11* (1), No. eadr4292.
(37) Schmaltz, T.; Hartmann, F.; Wicke, T.; Weymann, L.; Neef, C.; Janek, J. A Roadmap for Solid-State Batteries. *Adv. Energy Mater.* **2023**, *13* (43), 2301886.
(38) Lee, D.; Jung, H. Y.; Park, M. J. Solid-State Polymer Electrolytes Based on AB3-Type Miktoarm Star Copolymers. *ACS Macro Lett.* **2018**, *7* (8), 1046−1050.
(39) Petry, J.; Erabhoina, H.; Dietel, M.; Thelakkat, M. Comparative Study of the Mechanical Reinforcement by Blending, Filling, and Block Copolymerization in Bottlebrush Polymer Electrolytes. *ACS Appl. Polym. Mater.* **2024**, *6* (9), 5109−5120.
(40) Xu, P.; Wang, S.; Lin, A.; Min, H.-K.; Zhou, Z.; Dou, W.; Sun, Y.; Huang, X.; Tran, H.; Liu, X. Conductive and elastic bottlebrush elastomers for ultrasoft electronics. *Nat. Commun.* **2023**, *14* (1), 623.
(41) Liu, Y.; Zeng, Q.; Li, Z.; Chen, A.; Guan, J.; Wang, H.; Wang, S.; Zhang, L. Recent Development in Topological Polymer Electrolytes for Rechargeable Lithium Batteries. *Adv. Sci.* **2023**, *10* (15), 2206978.
(42) Glynos, E.; Petropoulou, P.; Mygiakis, E.; Nega, A. D.; Pan, W.; Papoutsakis, L.; Giannelis, E. P.; Sakellariou, G.; Anastasiadis, S. H. Leveraging Molecular Architecture To Design New, All-Polymer Solid Electrolytes with Simultaneous Enhancement in Modulus and Ionic Conductivity. *Macromolecules* **2018**, *51* (7), 2542−2550.
(43) Ji, X.; Xiao, L.; Zhang, Y.; Yue, K.; Zhou, X.; Guo, Z. Unveiling the Side-Chain Effect on Ionic Conductivity of Poly(ethylene Oxide)-Based Polymer-Brush Electrolytes. *ACS Appl. Energy Mater.* **2022**, *5* (7), 8410−8418.
(44) Butzelaar, A. J.; Röring, P.; Mach, T. P.; Hoffmann, M.; Jeschull, F.; Wilhelm, M.; Winter, M.; Brunklaus, G.; Théato, P. Styrene-Based Poly(ethylene oxide) Side-Chain Block Copolymers as Solid Polymer Electrolytes for High-Voltage Lithium-Metal Batteries. *ACS Appl. Mater. Interfaces* **2021**, *13* (33), 39257−39270.
(45) Zardalidis, G.; Pipertzis, A.; Mountrichas, G.; Pispas, S.; Mezger, M.; Floudas, G. Effect of Polymer Architecture on the Ionic Conductivity. Densely Grafted Poly(ethylene oxide) Brushes Doped with LiTf. *Macromolecules* **2016**, *49* (7), 2679−2687.
(46) Morioka, T.; Ota, K.; Tominaga, Y. Effect of oxyethylene side chains on ion-conductive properties of polycarbonate-based electrolytes. *Polymer* **2016**, *84*, 21−26.
(47) Isono, T. Synthesis of functional and architectural polyethers via the anionic ring-opening polymerization of epoxide monomers using a phosphazene base catalyst. *Polym. J.* **2021**, *53* (7), 753−764.
(48) Zeng, G.; Dai, S.; Chen, X.; Qiu, L.; Kong, X.; Huang, M.; Wen, T. Solid-State Graft Polymer Electrolytes with Conductive Backbones and Side Chains for Lithium Batteries. *Macromolecules* **2024**, *57* (3), 1258−1265.
(49) Nixon, K. D.; Sun, R.; Elabd, Y. A. Star poly(ionic liquid)s: Chain architecture-property relationships. *J. Polym. Sci.* **2024**, *62* (15), 3368−3380.
(50) Lapkriengkri, I.; Albanese, K. R.; Rhode, A.; Cunniff, A.; Pitenis, A. A.; Chabinyc, M. L.; Bates, C. M. Chemical Botany: Bottlebrush Polymers in Materials Science. *Annu. Rev. Mater. Res.* **2024**, *54*, 27−46.
(51) Daniel, W. F. M.; Burdyńska, J.; Vatankhah-Varnoosfaderani, M.; Matyjaszewski, K.; Paturej, J.; Rubinstein, M.; Dobrynin, A. V.; Sheiko, S. S. Solvent-free, supersoft and superelastic bottlebrush melts and networks. *Nat. Mater.* **2016**, *15* (2), 183−189.
(52) Nakano, S.; Piedrahita, C. R.; Onozuka, R.; Adachi, K.; Tsukahara, Y.; Pugh, C.; Kyu, T. Effect of Chain Architectures of Star-shaped Poly(ethylene glycol) Macromonomers on Enhancement of Thermal, Mechanical, and Electrochemical Performance of Polymer Electrolyte Membranes. *Chem. Lett.* **2018**, *47* (4), 587−590.
(53) Kim, J.-H.; Lee, K. M.; Kim, J. W.; Kweon, S. H.; Moon, H.-S.; Yim, T.; Kwak, S. K.; Lee, S.-Y. Regulating electrostatic phenomena by cationic polymer binder for scalable high-areal-capacity Li battery electrodes. *Nat. Commun.* **2023**, *14* (1), 5721.
(54) Zhang, X.; Cui, X.; Li, Y.; Yang, J.; Pan, Q. A Star-Structured Polymer Electrolyte for Low-Temperature Solid-State Lithium Batteries. *Small Methods* **2024**, *8* (12), 2400356.
(55) Kim, S.; Jeong, Y. H.; Won, G.; Jo, M. S.; Seo, S.; Kwon, D.-S.; Jeong, D.; Shim, J. Architecture-Tunable Bottlebrush Polymers as Artificial Solid Electrolyte Interphases for Lithium Metal Batteries. *Nano Lett.* **2025**, *25* (32), 12300−12308.
(56) Kang, J.; Eom, H.; Jang, S.; Yoo, D.; Lee, H.; Kim, M.; Seol, M. L.; Han, J. W.; Nam, I.; Song, H. Bollard-Anchored Binder System for High-Loading Cathodes Fabricated via Dry Electrode Process for Li-Ion Batteries. *Adv. Mater.* **2025**, *37* (12), No. e2416872.
(57) An, Y.; Yu, Q.; He, X.; Zheng, H.; Chen, J.; Zhu, S.; Wu, Q.; Zhao, Z. High-Electrochemical-Activity Composite Cathode Enabled by Fast Segmental Relaxation for Solid-State Lithium−Sulfur Batteries. *ACS Appl. Mater. Interfaces* **2024**, *16* (34), 44767−44779.
(58) Liu, H.; Wang, S.; Kong, W.; Liu, Y.; Wang, H. Constructing Ionic Transport Network via Supramolecular Composite Binder in Cathode for All-Solid-State Lithium Batteries. *Angew. Chem., Int. Ed.* **2025**, *64*, No. e202507579.
(59) Jin, B.; Cui, Z.; Manthiram, A. In Situ Interweaved Binder Framework Mitigating the Structural and Interphasial Degradations of High-nickel Cathodes in Lithium-ion Batteries. *Angew. Chem., Int. Ed.* **2023**, *62* (15), No. e202301241.
(60) Hu, J.; Wang, W.; Zhou, B.; Sun, J.; Chin, W. S.; Lu, L. Click Chemistry in Lithium-Metal Batteries. *Small* **2024**, *20* (7), No. e2306622.
(61) Olsén, P.; Odelius, K.; Albertsson, A.-C. Ring-Closing Depolymerization: A Powerful Tool for Synthesizing the Allyloxy-Functionalized Six-Membered Aliphatic Carbonate Monomer 2-Allyloxymethyl-2-ethyltrimethylene Carbonate. *Macromolecules* **2014**, *47* (18), 6189−6195.
(62) Zhang, J.; Liang, W.; Wen, L.; Lu, Z.; Xiao, Y.; Lang, M. Antibacterial AIE polycarbonates endowed with selective imaging capabilities by adjusting the electrostaticity of the mixed-charge backbone. *Biomater. Sci.* **2021**, *9* (15), 5293−5301.
(63) Thomas, A. W.; Kuroishi, P. K.; Pérez-Madrigal, M. M.; Whittaker, A. K.; Dove, A. P. Synthesis of aliphatic polycarbonates with a tuneable thermal response. *Polym. Chem.* **2017**, *8* (34), 5082−5090.
(64) Mindemark, J.; Imholt, L.; Montero, J.; Brandell, D. Allyl ethers as combined plasticizing and crosslinkable side groups in polycarbonate-based polymer electrolytes for solid-state Li batteries. *J. Polym. Sci., Part A: Polym. Chem.* **2016**, *54* (14), 2128−2135.
(65) Tudryn, G. J.; O'Reilly, M. V.; Dou, S.; King, D. R.; Winey, K. I.; Runt, J.; Colby, R. H. Molecular Mobility and Cation Conduction in Polyether−Ester−Sulfonate Copolymer Ionomers. *Macromolecules* **2012**, *45* (9), 3962−3973.
(66) Zapata-González, I.; Saldívar-Guerra, E.; Hutchinson, R. A. 80 years of the Mayo Lewis Equation. A Comprehensive Review on the Numerical Estimation Techniques for the Reactivity Ratios in Typical and Emerging Copolymerizations. *Prog. Polym. Sci.* **2025**, *163*, 101956.
(67) Beckingham, B. S.; Sanoja, G. E.; Lynd, N. A. Simple and Accurate Determination of Reactivity Ratios Using a Nonterminal Model of Chain Copolymerization. *Macromolecules* **2015**, *48* (19), 6922−6930.

https://doi.org/10.1021/acsapm.5c04494
ACS Appl. Polym. Mater. 2026, 8, 5459−5470

(68) Spyros, A.; Argyropoulos, D. S.; Marchessault, R. H. A. Study of Poly(hydroxyalkanoate)s by Quantitative 31P NMR Spectroscopy: Molecular Weight and Chain Cleavage. *Macromolecules* **1997**, *30* (2), 327−329.
(69) Wang, S.-W.; Colby, R. H. Linear Viscoelasticity and Cation Conduction in Polyurethane Sulfonate Ionomers with Ions in the Soft Segment−Multiphase Systems. *Macromolecules* **2018**, *51* (8), 2767−2775.
(70) Choi, U. H.; Colby, R. H. The Role of Solvating 12-Crown-4 Plasticizer on Dielectric Constant and Ion Conduction of Poly(ethylene oxide) Single-Ion Conductors. *Macromolecules* **2017**, *50* (14), 5582−5591.

https://doi.org/10.1021/acsapm.5c04494
ACS Appl. Polym. Mater. 2026, 8, 5459−5470